Vortex arrays directly generated from an efficient diode-pumped microchip laser

Journal of Physics: Photonics

OPEN ACCESS

RECEIVED
24 December 2019

REVISED
22 March 2020

ACCEPTED FOR PUBLICATION
17 April 2020

PUBLISHED
27 May 2020

PAPER

Vortex arrays directly generated from an efficient diode-pumped microchip laser

Dimeng Chen, Yujie Miao, Hanjie Wang and Jun Dong

Laboratory of Laser and Applied Photonics (LLAP), Department of Electronic Engineering, School of Electronic Science and Engineering, Xiamen University, Xiamen 361005, People's Republic of China

E-mail: jdong@xmu.edu.cn

Keywords: vortex array, microchip laser, phase singularity, orbital angular momentum

Abstract

Optical vortex arrays with multiple singularities arranged in distinct lattice structures provide more flexibility in trapping or manipulating microparticles, large-capacity optical communications and high-security information processing, and optical modulation. An efficient high-power compact laser with singularity-tunable vortex-array distribution is crucial for practical applications. Here, we directly generate various vortex arrays with tunable singularities from 1 to 10 in a microchip laser pumped with a tilted annular beam. Formation of vortex arrays in the microchip laser is achieved by manipulating the gain distribution in an Yb:YAG crystal by controlling the tilt angles and pump power. Efficient high-power laser operation with output power of 2.01 W and optical efficiency of 24.5% is obtained for a vortex array with 10 singularities. The pump-power-dependent saturated population inversion distribution plays a key role in generating vortex arrays formed with multi-transverse modes oscillating simultaneously in transverse-mode locking. The good agreement between theoretically simulated transverse patterns, phases and interference patterns for the vortex arrays and experimentally obtained results provides a solid foundation for developing efficient compact microchip lasers for generating vortex arrays by manipulating gain distribution in a thin medium pumped with a tilted annular beam.

1. Introduction

Vortex lasers carrying orbital angular momentum vertical-cavity surface-emitting [1] have been widely used in optical trapping [2], quantum communication [3], material processing [4], high-capacity storage [5], information processing [6], quantum entanglement [7], and high-resolution imaging [8]. Optical vortex arrays or vortex lattices [9–12] with multiple vortices arranged in a spatial distribution provide more flexible applications for trapping or manipulating microparticles [13–15], large-capacity optical communications and high-security information processing [16], optical modulation [17], etc. Therefore, various methods have been proposed for developing optical vortex arrays. Complex transverse patterns with spatially distributed vortices have been widely investigated theoretically and experimentally [18] since the concept of phase-singularity crystals was proposed [19]. Various phase-singularity crystals have been investigated theoretically based on the transverse-mode-locking effect in a frequency-degenerated family of modes, and demonstrated experimentally in an argon-ion laser pumped Na_2 molecular laser [19]. Various optical vortex crystals have been generated spontaneously in a semiconductor vertical-cavity surface-emitting laser [20]. However, the complexity of a vapor laser and low beam quality of a semiconductor laser have limited the applications of vortex arrays. Alternatively, optical vortices and vortex arrays have been generated by passing a single-mode laser through a specially designed spatial light modulator [7,17, 21–23], spiral phase plate [24], and hologram formed with liquid crystal [25]. However, the beam quality is degraded and transverse patterns are distorted because it is hard to achieve a highly precise process of the phase elements [26]. Diffraction loss and low damage threshold of these optical phase components also limit high power operation. Recently, various vortex-array beams have been generated in microchip lasers [9,12] and thin-slice solid-state lasers [27,28]. Square vortex arrays have been generated in a solid-state microchip laser with a

large Fresnel number by utilizing spontaneous mode locking and nonlinearity of the gain medium [12]. Vortex arrays have been generated in a thin-slice $LiNdP_4O_{12}$ solid-state laser by adjusting the pump beam shape and pump power [27]. Selective excitation of vortex arrays with hybrid Laguerre–Gaussian (LG), Hermite–Gaussian (HG) and Ince–Gaussian (IG) modes, such as $IG_{2,0}$–$LG_{0,2}$ and $HG_{2,1}$–$LG_{0,1}$ mode oscillating simultaneously, have been achieved in a wide-aperture laser-diode end-pumped thin-slice laser with a *c*-cut Nd:$GdVO_4$ crystal as the gain medium [28]. By adjusting the pump aperture and off-axis displacement of the laser diode to control the transverse-mode-locking effect, optical vortex lattice beams with phase-singularity arrays have been obtained in an *a*-cut thin-slice Yb:CALGO laser [29]. Manipulation of phase singularities has been demonstrated in a vortex array formed by coherently superposing two HG modes with spatial-energy mismatch [30]. Vortex arrays have been generated in an Yb:YAG/YVO_4 Raman microchip laser with the help of spatial modulation induced by the Raman conversion [31]. However, the optical efficiency is low because the off-axis pump induces mode mismatching between the laser and pump beams, and extra nonlinear elements introduce more losses.

Pump beams with annular-shaped distribution have been widely used for generating vortices in solid-state lasers [32–35]. However, the annular beams formed with mode-convert fiber [32, 33], axicon [34], and hollow focus lens [35] are less efficient because there are coupling and diffraction losses. Recently, by using a fiber-coupled laser-diode with an annular-shaped distribution as a pump source, high-beam-quality, efficient vector vortex lasers with different polarization states [36] and high-order cylindrical vector beams [37] have been demonstrated in Yb:YAG microchip lasers. Manipulation of orientation and separation between two vortices in a two-vortex array has been achieved in a passively Q-switched laser under decentered annular beam pumping [38]. Yb^{3+}-ion highly doped Yb:YAG crystals with high quantum efficiency and excellent spectral properties [39,40] have become one potential laser material for developing microchip lasers for generating vortex arrays.

Here, we report on direct generation of vortex arrays with tunable singularities up to 10 from a tilted annular-shaped laser-diode-pumped Yb:YAG microchip laser. Pump-power-dependent vortex-arrays beams with distinct phase-singularity distribution have been achieved. The output power was 2.01 W at an input pump power of 8.2 W. An optical efficiency of 24.5% was achieved. The vortex arrays with distinct singularity distribution are attributed to the simultaneous oscillation of two or three transverse modes with the transverse-mode-locking effect. The theoretically simulated results confirmed that asymmetrically elongated ring-shaped population inversion distribution was favorable for multiple transverse modes oscillating in the transverse-mode-locking state.

2. Experiments

The schematic of generating vortex arrays in a tilted annular-shaped fiber-coupled laser-diode-pumped microchip laser is shown in figure 1. The annular-shaped pump source and optics coupling system are the same as that used for generating high-order cylindrical vector beams [37]. The tilted annular-shaped laser-diode-pumped Yb:YAG microchip laser was realized by tilting the microchip laser head 5° with respect to the normal incident plane of the pump beam. The gain distribution is manipulated by focusing the annular beam 0.3 mm in an Yb:YAG crystal [41]. A 1 mm thick, coated Yb:YAG crystal doped with 10 at.% Yb^{3+} ions and a plane-parallel output coupler (OC) with 95% reflection were attached tightly to form microchip cavity. High reflection (HR) at 1030 nm and anti-reflection (AR) at 940 nm were coated on one surface of the Yb:YAG crystal to act as the rear cavity mirror (M1). The other surface of the Yb:YAG crystal was coated with AR at lasing wavelength to reduce diffraction and transmission losses. A beam profile analyzer (Thorlabs BC106-VIS) was employed for measuring the intensity profiles of the vortex-array beams. An Anritsu optical spectral analyzer (MS9740A) was used to measure the laser spectra of different vortex arrays.

3. Results

The lasers were examined under continuous-wave (CW) condition at input pump power (P_{in}) from 1 W to 8.2 W. The Yb:YAG microchip laser oscillated when P_{in} reached 1.7 W. The near-field intensity patterns generated experimentally at different P_{in}s were measured by transmitting the laser through a focus lens (100 mm focal length) on a beam profile analyzer. Within the available pump power range up to 8.2 W, 11 typical transverse patterns were obtained by adjusting the pump power. The intensity profiles remained as a Gaussian distribution when P_{in} increased from the threshold pump power to 2 W. One typical transverse pattern with Gaussian distribution at $P_{in} = 1.8$ W is shown in figure 2(a1). When P_{in} was increased over 2 W, the intensity profile changed from a Gaussian distribution to a doughnut. The pump power range for doughnut-shaped laser oscillation was from 2 W to 3.1 W. One typical doughnut-shaped laser profile at $P_{in} = 2.5$ W is shown in figure 2(b1). The experimentally obtained transverse patterns with Gaussian

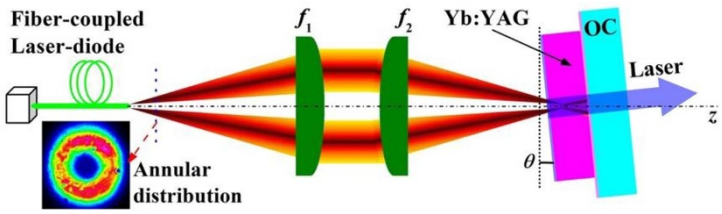

Figure 1. Experimental setup of an annular-shaped laser-diode-pumped Yb:YAG microchip laser for directly generating singularity-tunable vortex arrays. f_1 and f_2 are the collimating and focus lenses with a focal length of 8 mm. OC is the output coupler. θ is the tilt angle of the Yb:YAG crystal with respect to the annular pump beam. The inset shows the measured annular intensity profile from a fiber-coupled laser diode.

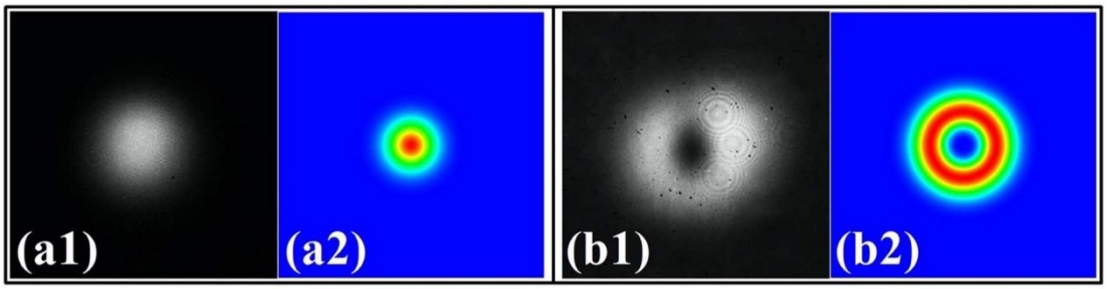

Figure 2. Typical transverse patterns of Gaussian distribution and doughnut profile obtained experimentally in the microchip laser at (a1) $P_{in} = 1.8$ W and (b1) $P_{in} = 2.5$ W. (a2) Theoretical simulated intensity distribution of TEM_{00} mode; (b2) theoretical simulated intensity distribution of $LG_{0,1}$ mode.

distribution and doughnut profile, as shown in figures 2(a1) and (b1), are in good agreement with the theoretical simulated TEM_{00} mode and $LG_{0,1}$ mode, as shown in figures 2(a2) and (b2).

Further increasing P_{in} over 3.1 W, the near-field transverse profile changed from a doughnut pattern to complex transverse patterns characterized by arrays of vortices with null intensities, namely, vortex-arrays. Figure 3 shows the typical vortex-arrays experimentally generated in the Yb:YAG microchip laser at different P_{in}s, together with the schematic distribution of the vortices. A two-vortex array consisting of two separated vortices was observed when P_{in} was higher than 3.1 W; one example at $P_{in} = 3.5$ W is shown in figure 3(a). A three-vortex array consisting of three vortices arranged along a line was obtained when P_{in} reached 4 W. One example of a three-vortex array at $P_{in} = 4.2$ W is shown in figure 3(b). A four-vortex array with four vortices in a diamond shape was obtained when P_{in} increased to 4.6 W. One typical four-vortex array obtained experimentally at $P_{in} = 4.8$ W is shown in figure 3(c). When P_{in} reached over 5.1 W, the laser oscillated in a five-vortex array consisting of five vortices arranged as a vortex surrounded by four vortices in a rectangular structure. A typical five-vortex array at $P_{in} = 5.2$ W is shown in figure 3(d). A six-vortex array consisting of six vortices in a doubled diamond structure was generated when P_{in} was higher than 5.6 W. A typical six-vortex array at $P_{in} = 6$ W is shown in figure 3(e). A seven-vortex array consisting of seven vortices arranged as a vortex centered in a distorted hexagon was obtained when P_{in} was higher than 6.4 W. A typical seven-vortex array at $P_{in} = 6.5$ W is shown in figure 3(f). An eight-vortex array consisting of eight vortices arranged in a lattice with two vortices between two lines of three vortices was observed when P_{in} was higher than 6.9 W. One example of an eight-vortex array at $P_{in} = 7$ W is shown in figure 3(g). A nine-vortex-array consisting of nine vortices in a lattice structure was obtained when P_{in} was higher than 7.3 W. One typical nine-vortex array at $P_{in} = 7.5$ W is shown in figure 3(h). A ten-vortex-array consisting of ten vortices arranged as two separated vortices surrounded by an octagon was achieved as P_{in} reached 8.1 W. One typical ten-vortex-array at $P_{in} = 8.2$ W is shown in figure 3(i).

The threshold pump powers (P_{th}) for different vortex arrays were determined by slowly adjusting P_{in} for observing the transition from one transverse pattern to another. The transition from one transverse pattern to another is sudden and abrupt owing to the pump-power-dependent transverse mode competition. However, the observed transverse patterns are stable once the transverse patterns are generated. Figure 4 depicts the variation of P_{th}s for different vortex arrays with vortex number (m), together with the P_{th}s for TEM_{00} and doughnut modes. The P_{th} for TEM_{00} mode was 1.7 W, and the P_{th} for doughnut mode was 2 W. A near-linear increase of P_{th} with vortex number was observed for the vortex arrays. The increased rate of P_{th} is about 0.6 W per vortex number. Wide separation of the threshold pump powers between two adjacent

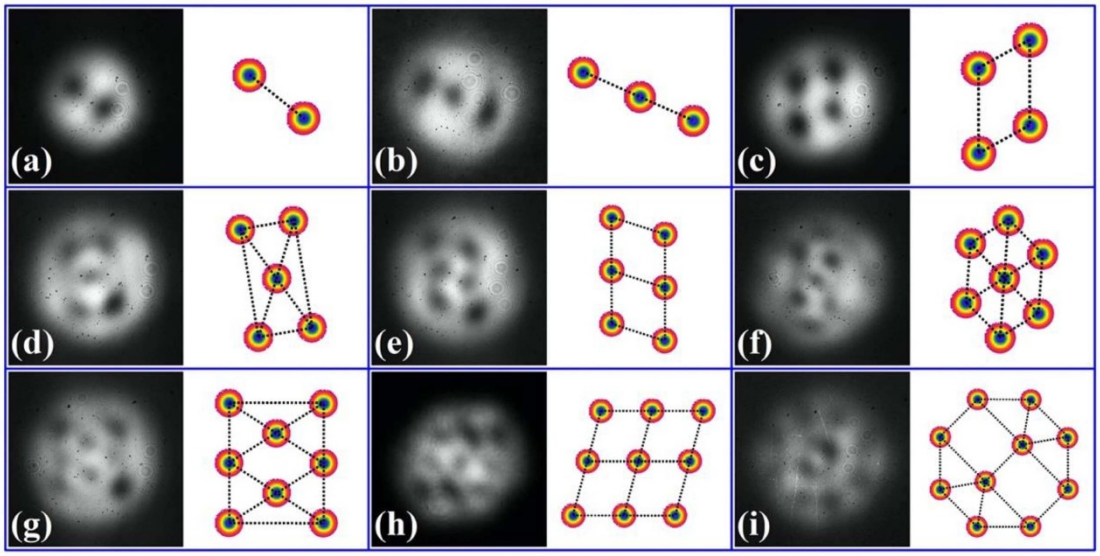

Figure 3. Typical transverse intensity profiles of vortex arrays with distinct lattice structures experimentally obtained in the Yb:YAG microchip laser at different P_{in}s. (a) $P_{in} = 2$ W, (b) $P_{in} = 3.1$ W, (c) $P_{in} = 4$ W, (d) $P_{in} = 4.6$ W, (e) $P_{in} = 5.2$ W, (f) $P_{in} = 5.6$ W, (g) $P_{in} = 6.6$ W, (h) $P_{in} = 7$ W, (i) $P_{in} = 7.3$ W, (j) $P_{in} = 8.1$ W. The spatial distributions of the vortices for different vortex arrays are given alongside the corresponding vortex arrays.

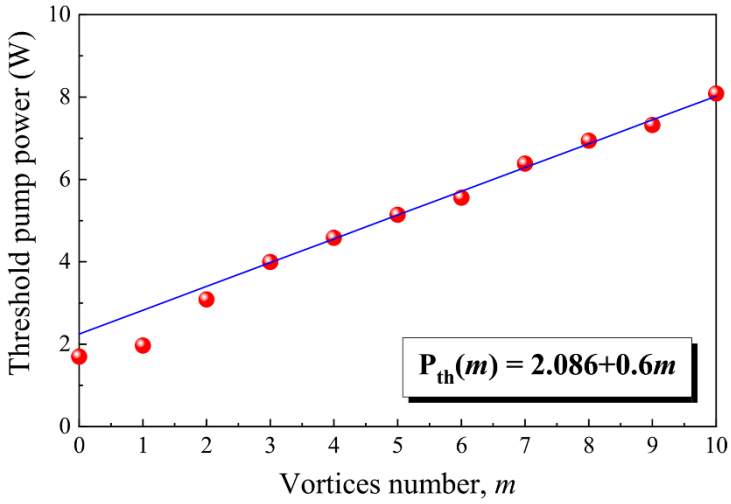

Figure 4. Threshold pump powers of vortex arrays generated in the Yb:YAG microchip laser as a function of vortex number, m. The threshold pump powers of TEM_{00} and doughnut modes are also given for comparison. The solid line is the linear fit of the experimental data.

vortex arrays is more favorable for maintaining stable operation of a specific vortex-array beam generated in the compact microchip laser. Vortex-number-controllable vortex arrays with wide pump power range provide more flexibility for various applications and are favorable for developing a compact laser.

The phase helicities of the vortex arrays obtained in the microchip laser were verified with interference experiments. A plane-wave reference beam was formed by spatially selecting a tiny portion of a vortex-array beam, and then interfering with the vortex-array beams to generate interference patterns. The interference pattern was captured with a beam profile analyzer. Figure 5 shows the experimentally obtained interference patterns of some vortex arrays emitted by the microchip laser (doughnut, two-vortex array, three-vortex array, four-vortex array, five-vortex array, six-vortex array). As shown in figure 5(a), the bifurcated forklike interference pattern clearly confirms that the doughnut beam is an optical vortex beam processing a phase singularity. The topological charge is ± 1 depending on the helicity of the vortex beam. For the two-vortex-array beam, as shown in figure 5(b), two bifurcated forklike interference fringes verify that the two-vortex-array beam has two phase singularities. Each vortex has unitary topological charge. However, the phase helicities of the two vortices are opposite, thus the total charge of the two-vortex beam is 0. Similarly, the three-vortex-array beam processes three phase singularities each of unitary charge, and the total charge is

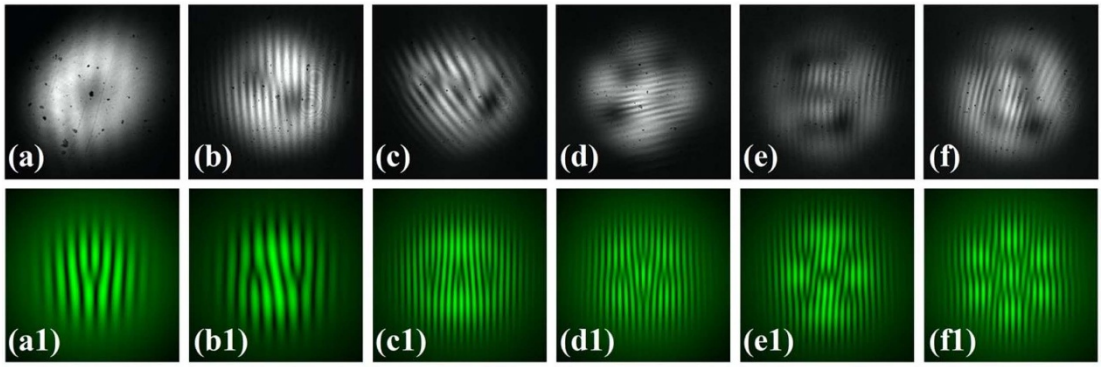

Figure 5. Experimentally obtained interference patterns of vortex arrays interfering with a plane-wave reference beam at different P_{in}s: (a) $P_{in} = 2$ W, (b) $P_{in} = 3.1$ W, (c) $P_{in} = 4$ W, (d) $P_{in} = 4.6$ W, (e) $P_{in} = 5.2$ W. (a1)–(f1) Theoretical simulated interference patterns for vortex arrays.

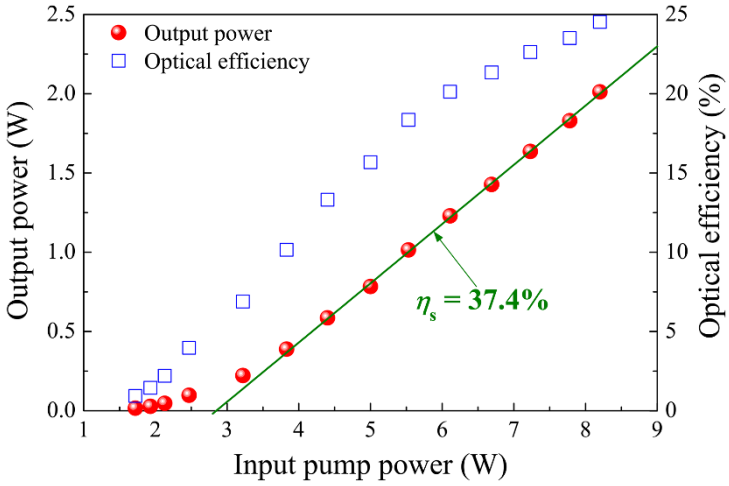

Figure 6. Output power and optical efficiency of Yb:YAG microchip laser vs. P_{in}. The solid line is the linear fit of the experimental data of output power.

± 1, as shown in figure 5(c). The four-vortex array processes four singularities, and the total charge is 0, as shown in figure 5(d). As shown in figures 5(e) and (f), the measured interference patterns of the five-vortex array and six-vortex array clearly show that they possess five singularities and six singularities, each of unitary charge, and the total charges are ± 1 and 0, respectively. Therefore, for the vortex arrays with even phase singularities such as 2, 4, 6, the total charge is 0; while for the vortex arrays with odd phase singularities such as 1, 3, 5, the total charge is ± 1. The same phenomena were observed for the vortex arrays with vortex number larger than 6 generated in the microchip laser. The interference results further confirmed that the experimentally obtained transverse patterns (figure 3) are vortex arrays with structured distributed vortices, and each vortex possesses unitary topological charge.

Figure 6 depicts the relationship between the output power and P_{in} for the microchip laser, together with the variation of optical efficiency with P_{in}. The P_{th}s for TEM_{00} and doughnut modes are 1.7 W and 2 W, respectively. Although the transverse intensity profile of the microchip laser changed with P_{in} (as shown in figure 3), the output power of the vortex-array laser increased linearly with P_{in} when P_{in} was higher than 3 W. The increase rate of output power with P_{in} (slope efficiency) was approximately 37.4%. A maximum output power of 2.01 W was achieved at $P_{in} = 8.2$ W. The corresponding optical efficiency of 24.5% was 40% higher than that obtained in high-order cylindrical vector beam lasers [37]. No output power degradation was observed within the available maximum pump power. This indicates that the output power could be scaled by applying high pump power. It is also possible to generate vortex arrays with phase singularities larger than 10 because high-order LG modes are favorable for oscillation to form a vortex array with large vortex number at high pump power supplied from an annular pump beam. The highly efficient performance of the tilted annular-shaped laser-diode-pumped Yb:YAG microchip laser was mainly caused by the transverse-mode-locking effect. The population inversion distributed along the Yb:YAG crystal length

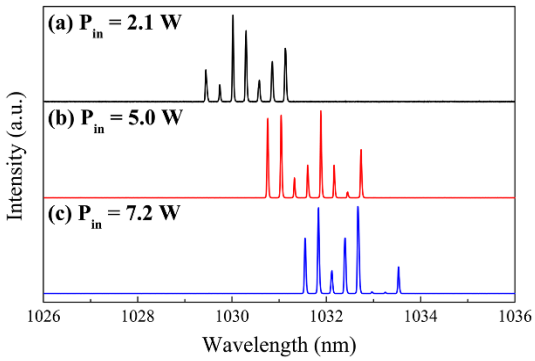

Figure 7. Typical oscillation spectra of the microchip laser at different P_{in}s.

excited by the tilted focused annular beam is fully utilized by different participating transverse modes; therefore, stationary vortex arrays are formed with multiple transverse modes oscillating simultaneously in transverse-mode-locking state.

The measured laser spectra at different P_{in}s show that multi-longitudinal-mode oscillation around 1030 nm is dominant in the Yb:YAG microchip laser owing to the broad emission spectrum of the Yb:YAG crystal at approximately 1.03 μm [42]. Figure 7 depicts some typical oscillation spectra at different P_{in}s. From the oscillation spectrum shown in figure 7(a), we can see that seven longitudinal modes oscillate at $P_{\mathrm{in}} = 2.1$ W. The longitudinal modes increase to 8 when P_{in} is higher than 4.5 W. The eight-longitudinal-mode oscillation is maintained with further increasing of P_{in}, as shown in figure 7(b) at $P_{\mathrm{in}} = 5$ W and figure 7(c) at $P_{\mathrm{in}} = 7.2$ W. The oscillation spectrum shifts to longer wavelength as P_{in} increases, as shown in figure 7. The intensities of longitudinal modes also vary at different P_{in}s because there is longitudinal mode competition. The separation between two consecutive longitudinal modes is 0.29 nm, which is in good agreement with the free spectral range (0.291 nm) of the microchip laser cavity filled with 1 mm Yb:YAG crystal. The frequency separation between the consecutive longitudinal modes is $\Delta\nu_{\mathrm{L}} = c/2L$, where c is the speed of light in a vacuum, and L is the resonator optical length. The frequency separation between the consecutive transverse modes is $\Delta\nu_{\mathrm{T}} = \Delta\nu_{\mathrm{L}}\left[\frac{1}{\pi}\Delta\left(2p+l\right)\arccos\left(1-\frac{L}{R}\right)\right]$ [43], where p and l are the indices of a particular transverse mode, and R is the radius of curvature of the mirror. For the present plane-parallel microchip laser resonator, R is very large compared to L; therefore, the frequency separation between the transverse modes participating in forming a vortex array in the Yb:YAG microchip is small. $\Delta\nu_{\mathrm{T}}$ is several orders of magnitude lower than $\Delta\nu_{\mathrm{L}}$. Thus, the resonant-mode spectrum is composed of the relatively large longitudinal mode spacing $c/2L$, with each longitudinal mode surrounded by a set of transverse-mode resonances. The oscillation spectra with relatively stable multi-longitudinal-mode oscillations indicate that the transverse-mode-locking effect is responsible for forming stationary vortex-array transverse patterns in the Yb:YAG microchip laser pumped with a tilted annular beam. The multi-longitudinal-mode oscillation of the Yb:YAG microchip laser may cause some fluctuations in the laser output power and vortex arrays because the pulsation exists for each longitudinal mode [12]. It is possible to obtain stable oscillation in the Yb:YAG microchip laser due to the higher number of longitudinal modes extracting the energy for available manipulated gain distribution provided by the tilted annular pump beam.

4. Theoretical modeling

A microchip laser is a high-quality resonator filled with a high-nonlinearity gain medium. Its short cavity and large unrestricted lateral dimension enable a large Fresnel number $({w_{\mathrm{p}}}^2/(\lambda L_{\mathrm{c}}))$, where w_{p} is the effective pump beam radius, λ is the laser wavelength, and L_{c} is the gain thickness. The Fresnel number of the microchip laser further increases with the effective pump beam diameter. A microchip laser with a large Fresnel number is favorable for high-order $\mathrm{LG}_{p,l}$ mode oscillation. For a microchip laser pumped with a tilted annular beam, formation of vortex arrays is attributed to the asymmetrically distributed saturated population inversion inside the gain medium. The asymmetrically distributed saturated population inversion along the thickness and radial direction inside the gain medium provides possibilities for different $\mathrm{LG}_{p,l}$ modes oscillating simultaneously. For a focused annular pump beam [37] tilted by an angle θ, the normalized pump power distribution can be expressed as follows [38]:

$$R_{\mathrm{p}}(r,z)=\frac{\alpha}{\pi w_{\mathrm{p}}^{2}(z\cos\theta+r\sin\theta)}\frac{\exp\left[-\alpha(z\cos\theta+r\sin\theta)\right]}{\left[1-\exp\left(-\alpha L_{\mathrm{c}}/\cos\theta\right)\right]}\times\left[\exp\left(\frac{-2(r\cos\theta-z\sin\theta-r_{0})^{2}}{w_{\mathrm{p}}^{2}(z\cos\theta+r\sin\theta)}\right)+\exp\left(\frac{-2(r\cos\theta-z\sin\theta+r_{0})^{2}}{w_{\mathrm{p}}^{2}(z\cos\theta+r\sin\theta)}\right)\right] \tag{1}$$

where α and L_{c} are the absorption coefficient and gain thickness, $w_{\mathrm{p}}(z)$ is the position-dependent radius of the TEM_{00} laser beam, $r_0=|z-z_0|\tan(\theta_{\mathrm{p}})$ is the offset distance between the TEM_{00} beam and propagation direction, $2\theta_{\mathrm{p}}$ is the annular beam divergence angle, and z_0 is the position of the focus spot.

Owing to the tightly focusing properties of the annular beam, pump saturation effect at the focus spot has to be considered for estimating population inversion. Therefore, the P_{in}-dependent saturated population inversion taking into account the pump saturation effect can be expressed as

$$\Delta N(r,z)=\frac{R_{\mathrm{p}}(r,z)\,\tau\left(1-e^{-\alpha L_{\mathrm{c}}/\cos\theta}\right)P_{\mathrm{in}}}{h\nu_{\mathrm{p}}\left(1+I_{\mathrm{p}}(r,z)/I_{\mathrm{s}}\right)} \tag{2}$$

$$I_{\mathrm{p}}(r,z)=\frac{P_{\mathrm{in}}e^{-\alpha(z\cos\theta+r\sin\theta)}}{\pi w_{\mathrm{p}}^{2}(z\cos\theta+r\sin\theta)}\exp\left[\frac{-2(r\cos\theta-z\sin\theta)^{2}}{w_{\mathrm{p}}^{2}(z\cos\theta+r\sin\theta)}\right] \tag{3}$$

where I_{s} is the saturated pump power intensity, and $I_{\mathrm{p}}(r,z)$ is the pump power intensity.

We defined the effective population inversion as the average distribution of the population inversion inside the gain medium. The effective population inversion distribution along the radial coordinate can be expressed as [38]

$$\Delta N_{\mathrm{eff}}(x,y)=\frac{\int_{0}^{L_{\mathrm{c}}}\Delta N(x,y,z)\,dz}{L_{\mathrm{c}}}. \tag{4}$$

Firstly, we theoretically investigate the effects of the annular beam tilting angle (θ) on the distribution of saturated population inversion inside the gain medium. Figure 8 shows the calculated saturated population inversion along the thickness and radial direction inside an Yb:YAG crystal at different θs. The parameters of the Yb:YAG crystal ($\alpha=10\ \mathrm{cm}^{-1}$, $L_{\mathrm{c}}=1$ mm) and pump beam ($w_{\mathrm{p0}}=20\ \mu$m, $\theta_{\mathrm{p}}=10^{\circ}$, $z_0=0.3$ mm) are used in the theoretical calculations. P_{in} was set to 8 W in the theoretical calculation. When the incident angle of the annular beam is 0° (normally incident on the Yb:YAG crystal), the saturated population inversion is distributed symmetrically along the thickness (see figure 8(a1)). The effective population inversion is a ring shape, as shown in figure 8(a2). When the annular beam is tilted 2° respective to the normal of the crystal surface, the saturated population inversion along the thickness is distorted (see figure 8(b1)). The distribution of the effective population inversion is changed from a symmetrical ring shape to a distorted ring shape with uneven population inversion distribution around the ring. As shown in figure 8(b2), there are two crescents with inversion population higher than $8\times10^{20}\ \mathrm{cm}^{-3}$ for illustration. The saturated population inversion along the thickness of the Yb:YAG crystal is distorted with an increase in θ, as shown in figures 8(c1)–(e1). The effective population inversion distribution also tends to be further distorted with an increase in θ, as shown in figures 8(c2)–(e2). The highest effective population inversion increases with θ because the absorption of the pump power is proportional to the effective absorption length of the gain medium ($L_{\mathrm{c}}/\cos\theta$). The distribution of the effective population inversion further elongates along the y-axis and shrinks along the x-axis, as shown in figures 8 (c2)–(e2). Thus, the distribution of the effective population inversion excited in the Yb:YAG crystal can be manipulated by adjusting the tilt angle of the annular pump beam. Owing to the tightly focusing properties of the annular beam, the pump saturation effect around the focal spot further expands the distribution of the population inversion through the gain guiding effect. Therefore, the tilt-angle-dependent population inversion distribution provides an arena for multi-transverse modes oscillating simultaneously to form various stationary vortex arrays in the Yb:YAG microchip laser pumped with a tilted annular beam.

For the Yb:YAG microchip laser pumped with a tilted annular beam (as shown in figure 1), oscillation of TEM_{00}, doughnut mode, and stationary vortex arrays are determined by the population inversion distribution in the Yb:YAG crystal, which relies on the applied pump power. Figure 9 shows the calculated population inversion along the thickness and radial direction in the Yb:YAG crystal at different P_{in}s. The tilt angle of the annular beam, θ, was set to 5° in the theoretical calculation. A red contour line ($4\times10^{20}\ \mathrm{cm}^{-3}$) and black contour line ($8\times10^{20}\ \mathrm{cm}^{-3}$) are plotted to indicate the change of the pump areas with P_{in}, as

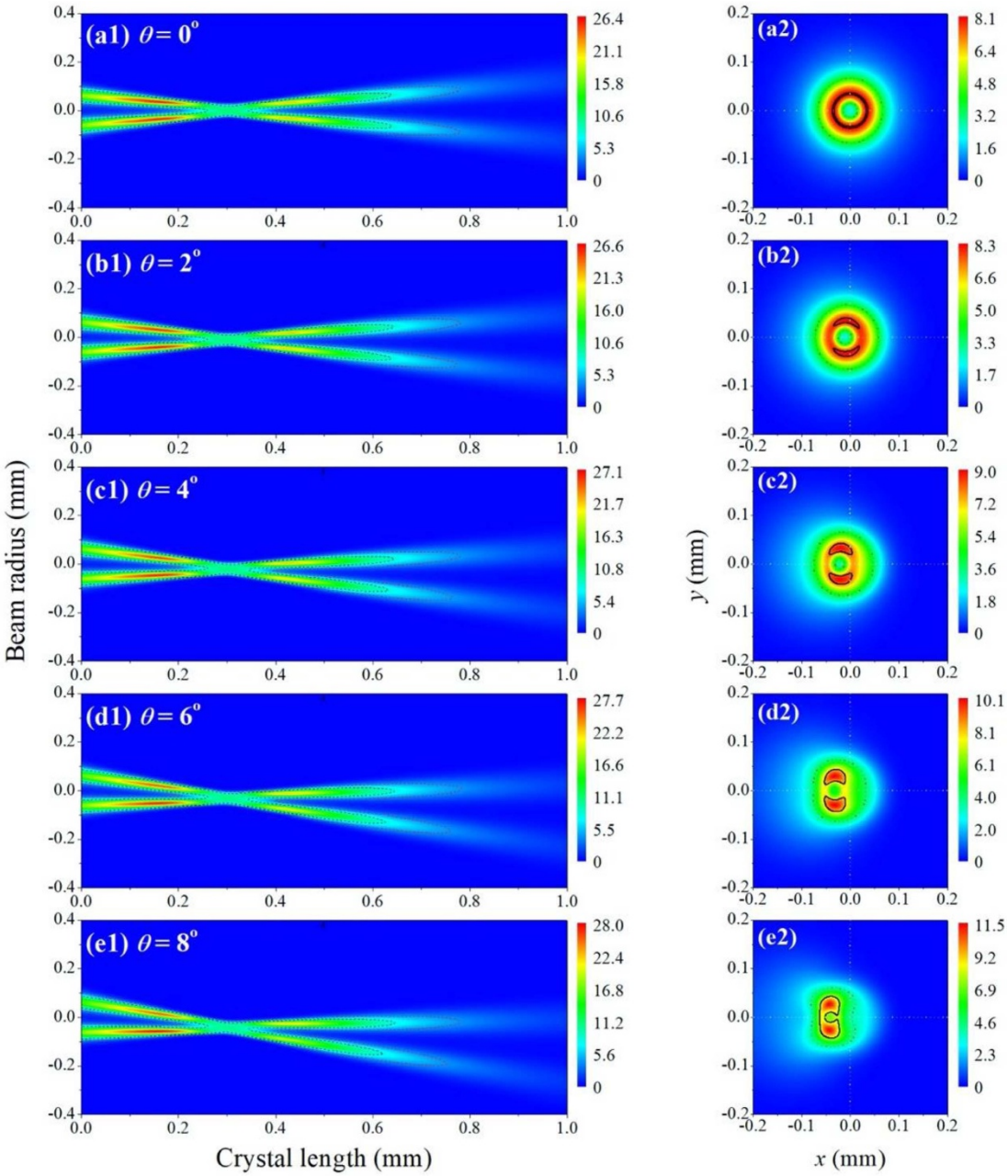

Figure 8. Saturated population inversion distribution along the thickness of the Yb:YAG crystal at different tilt angles (a1)–(e1) and the corresponding effective population inversion distribution (a2)–(e2). An incident pump power of 8 W is used in the theoretical calculations.

shown in figures 9(a1)–(d1). The effective absorption length of the Yb:YAG crystal (population inversion $> 4 \times 10^{20}$ cm^{-3}) increases with P_{in}. Besides the contribution to population inversion $> 8 \times 10^{20}$ cm^{-3} coming from around the focus spot, the pumped area (population inversion $> 8 \times 10^{20}$ cm^{-3}) enlarges with an increase in P_{in}. The effective population inversion distribution (figure 9(a2)) is an elongated ring with comparable population inversion, which is sufficient for supporting TEM_{00}-mode oscillation. With further increasing P_{in}, the pump saturation effect around the focus spot has a great effect on the distribution of the population inversion. The effective population inversion distribution tends to be an elongated ring along the y-axis with increasing P_{in}, as shown in figures 9(b2)–(d2). Further increasing P_{in}, the pumped area (population inversion $> 8 \times 10^{20}$ cm^{-3}) is enlarged (see figure 9(b1) at $P_{in} = 4$ W). The effective population inversion distribution is an elongated ring with relatively low inversion population around the center, as shown in figure 9(b2). The population inversion increases with further increasing P_{in}; see figure 9(c1) at $P_{in} = 6$ W and figure 9(d1) at $P_{in} = 8$ W. The corresponding effective population inversion distribution exhibits an elongated ring with enlarged central area, as shown in figures 9(c2) and (d2). As shown in figure 9, the pump-power-dependent elongated ring distribution of effective

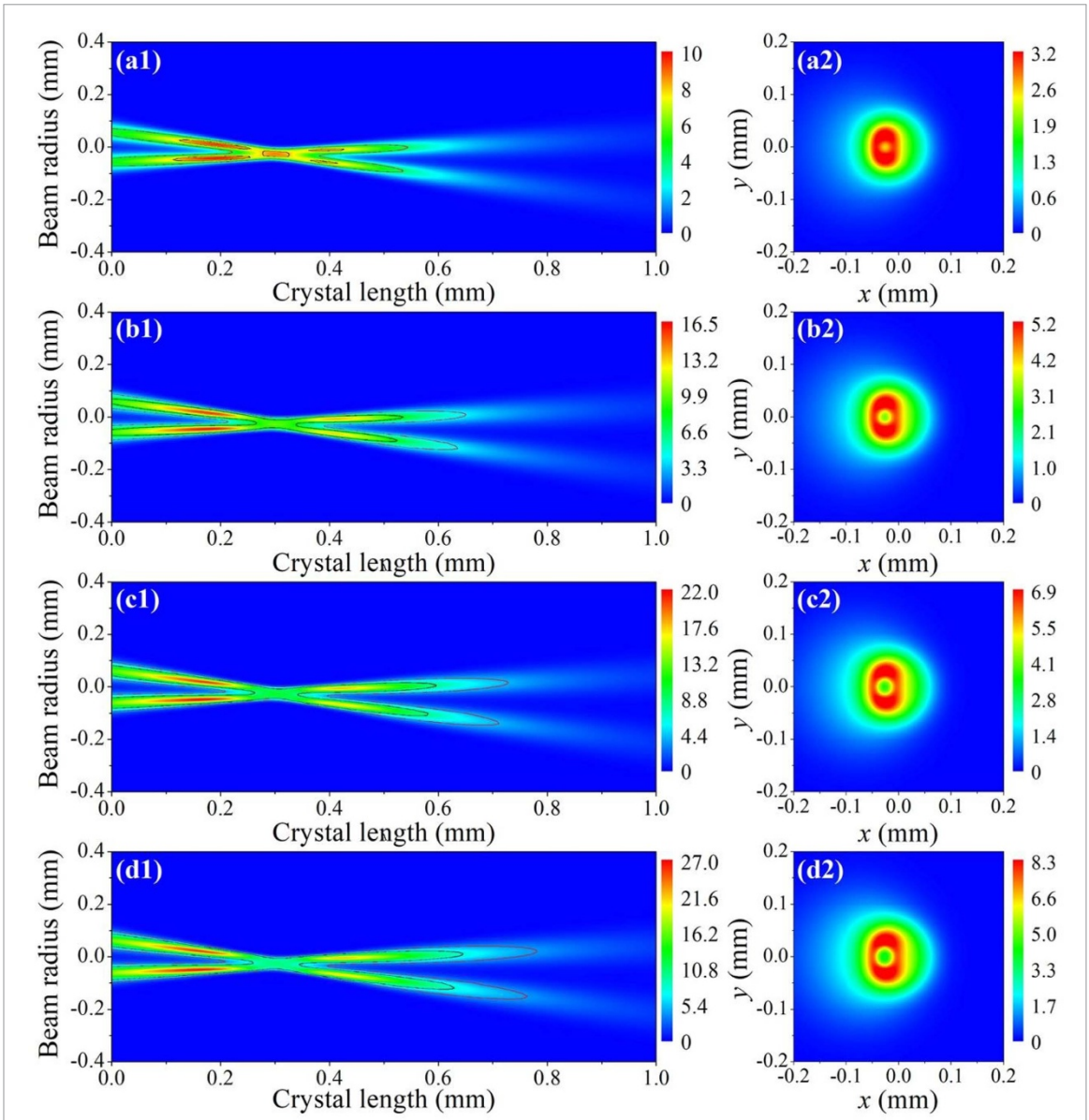

Figure 9. Theoretically calculated saturated population inversion distribution in a 1 mm thick Yb:YAG crystal pumped with a tilted annular beam at different P_{in}s: (a1) $P_{in} = 2$ W, (b1) $P_{in} = 4$ W, (c1) $P_{in} = 6$ W, (d1) $P_{in} = 8$ W. The tilt angle is 5°. (a2)–(d2) Corresponding effective inversion population distribution inside the Yb:YAG crystal at different P_{in}s.

population inversion provides an arena for simultaneous oscillation of different $LG_{p,l}$ modes in the Yb:YAG microchip laser pumped with a tilted annular beam. Various stationary vortex arrays are formed with transverse-mode-locking effect if the population inversion is sufficient to overcome the lasing thresholds of selected $LG_{p,l}$ modes. Therefore, it is reasonable in theory to generate vortex arrays in the Yb:YAG microchip laser pumped with a tilted annular beam.

The oscillation of various LG modes depends on the mode coupling between the population inversion distribution and the distribution of LG modes. The transverse distribution of LG modes can be described with equations (5) and (6). The beam waist of the $LG_{p,l}$ modes is defined as the $1/e^2$ intensity points of the outermost lobe, and increases with p and l. The oscillation of $LG_{p,l}$ modes with different beam waists and beam profiles depends on the gain distribution excited in the gain medium. Therefore, it is possible to form stationary transverse patterns with different transverse modes of oscillation simultaneously by manipulating the gain distribution inside the laser medium. Figure 10 depicts the profile distribution of the possible participating transverse modes for forming pump-power-dependent vortex arrays in the Yb:YAG microchip laser pumped with a tilted annular beam. The effective population inversion distribution is concentrated at low pump power, as shown in figure 9(a1), which is favorable for TEM_{00}-mode laser oscillation (figure 10(a)). Owing to the enhanced pump saturation effect with an increase in pump power, the effective population inversion at the center increases slowly compared to that around the ring (figure 9(b2)). The gain for the TEM_{00} mode decreases while the gain distribution is favorable for $LG_{0,1}$-mode oscillation (see

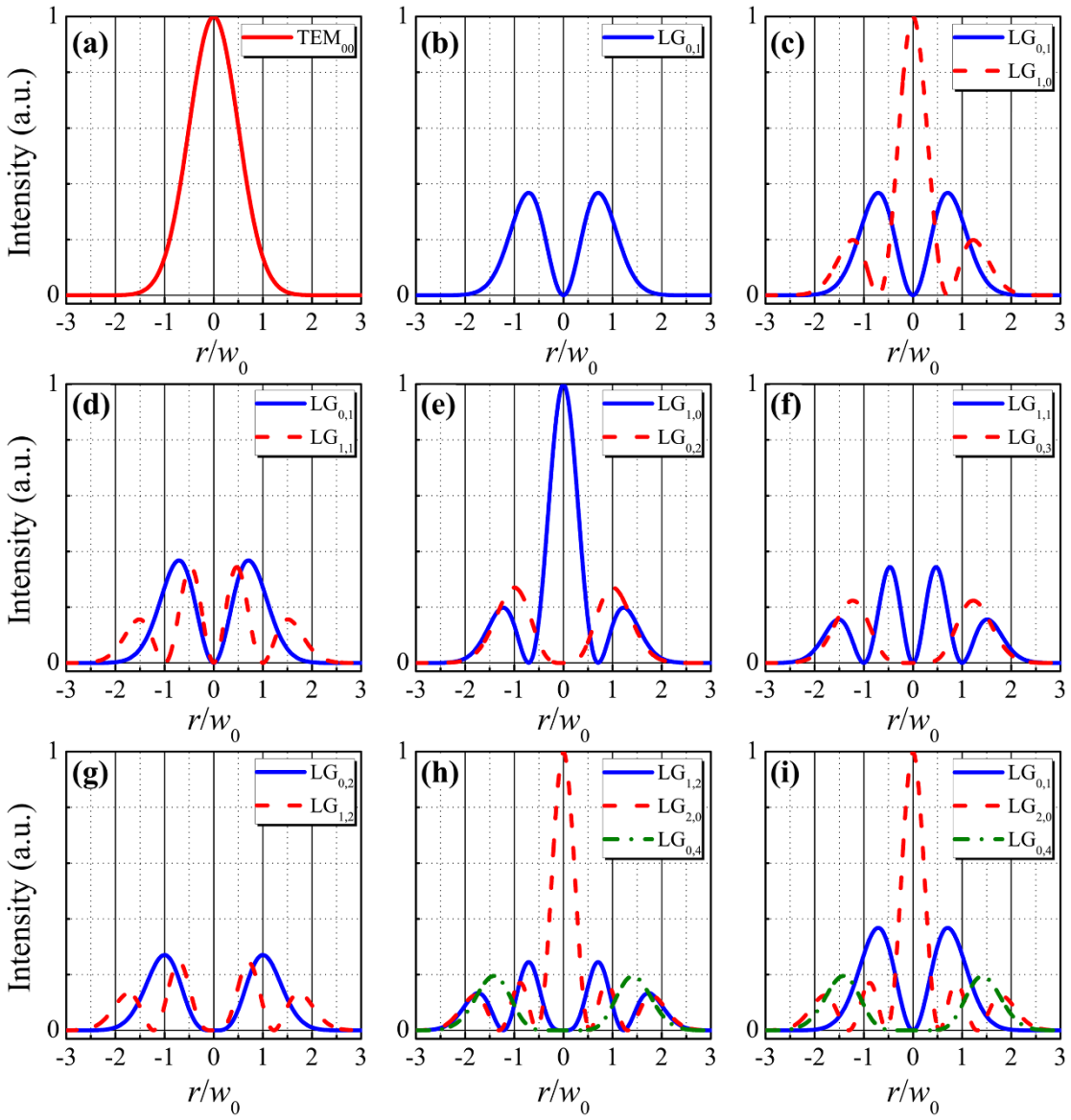

Figure 10. Transverse distribution of possible oscillating modes for forming vortex arrays in the Yb:YAG microchip laser pumped with a tilted annular beam. (a) TEM_{00}, (b) $LG_{0,1}$, (c) $LG_{0,1} + LG_{1,0}$, (d) $LG_{0,1} + LG_{1,1}$, (e) $LG_{1,0} + LG_{0,2}$, (f) $LG_{1,1} + LG_{0,3}$, (g) $LG_{0,2} + LG_{1,2}$, (h) $LG_{1,2} + LG_{2,0} + LG_{0,4}$, (i) $LG_{0,1} + LG_{2,0} + LG_{0,4}$. The radii are normalized to the beam waist of the fundamental mode, $w_{0.}$

figure 10(b)); therefore, $LG_{0,l}$ mode oscillates rather than TEM_{00} mode. The effective population inversion distribution further elongates along the *y*-axis with further increasing pump power. The doughnut modes ($LG_{0,l}$, L $G_{0,-1}$) oscillate together with $LG_{1,0}$ mode owing to the increase in population inversion at the center with P_{in}, as shown in figure 10(c). Therefore, a two-vortex array is formed with two opposite unitary phase singularities. With increasing P_{in}, the enhanced saturated population inversion distribution is favorable for oscillation of two orthogonal doughnut modes ($LG_{0,1}$ and $LG_{0,-1}$) together with two orthogonal $LG_{1,1}$ and $LG_{1,-1}$ modes, as shown in figure 10(d), thus a three-vortex array is formed. With further increase in P_{in}, the effective population inversion distribution is expanded for high-order-mode oscillation. Therefore, the transverse modes such as $LG_{0,1}$, $LG_{1,0}$, $LG_{0,2}$, $LG_{1,1}$, $LG_{0,3}$, $LG_{2,0}$, $LG_{1,2}$ and $LG_{0,4}$ modes compete for the gain to form pump-power-dependent vortex arrays. As shown in figures 10(e)–(i), the formation of vortex arrays with certain transverse modes is determined by the pump-power-dependent saturated population inversion distribution in the Yb:YAG microchip laser pumped with a tilted annular beam.

The vortex arrays formed with transverse-mode-locking effect can be expressed with a linear combination of $LG_{p,l}$ modes with near frequency-degenerated mode locking. The electrical fields of $LG_{p,l}$

Table 1. Possible transverse modes oscillating simultaneously to form vortex arrays in theoretical simulations.

	Participating transverse modes and their weights for forming vortex arrays				
Singularity	$g_1 \times E_{p1,0}$	$g_2 \times E_{p2,l2}$	$g_3 \times E_{p2,-l2}$	$g_4 \times E_{p3,l3}$	$g_5 \times E_{p3,-l3}$
1		$1 \times E_{0,1}(r,\phi)$			
2	$1.6 \times E_{1,0}(r,\phi)$	$1 \times E_{0,1}(r,\phi)$	$1 \times E_{0,-1}(r,\phi)$		
3		$1 \times E_{0,1}(r,\phi)$	$1 \times E_{0,-1}(r,\phi)$	$1 \times E_{1,1}(r,\phi)$	$0.4 \times E_{1,-1}(r,\phi)$
4	$1 \times E_{1,0}(r,\phi)$	$0.3 \times E_{0,2}(r,\phi)$	$0.5 \times E_{0,-2}(r,\phi)$		
5		$1 \times E_{0,3}(r,\phi)$	0	$0.05 \times E_{1,1}(r,\phi)$	$0.8 \times E_{1,-1}(r,\phi)$
6		$1 \times E_{0,2}(r,\phi)$	$1 \times E_{0,-2}(r,\phi)$	$1 \times E_{1,2}(r,\phi)$	$1 \times E_{1,-2}(r,\phi)$
7		$0.8 \times E_{0,3}(r,\phi)$	$0.4 \times E_{0,-3}(r,\phi)$	$-0.6 \times E_{1,1}(r,\phi)$	$1 \times E_{1,-1}(r,\phi)$
8	$1 \times E_{2,0}(r,\phi)$	$1 \times E_{0,4}(r,\phi)$	$0.1 \times E_{0,-4}(r,\phi)$	$0.5 \times E_{1,2}(r,\phi)$	$0.5 \times E_{1,-2}(r,\phi)$
9		$0.01 \times E_{0,3}(r,\phi)$	$0.55 \times E_{0,-3}(r,\phi)$	$1 \times E_{1,1}(r,\phi)$	$0.01 \times E_{1,-1}(r,\phi)$
10	$1 \times E_{2,0}(r,\phi)$	$0.2 \times E_{0,1}(r,\phi)$	$0.3 \times E_{0,-1}(r,\phi)$	$0.6 \times E_{0,4}(r,\phi)$	$0.6 \times E_{0,-4}(r,\phi)$

modes, $A_{p,l}(r,\phi)$, can be expressed as follows:

$$A_{p0}(r,\phi) = \frac{2}{\sqrt{2\pi}} L_p^0\left(\frac{2r^2}{w_0^2}\right)\exp\left(\frac{-r^2}{w_0^2}\right) \tag{5}$$

$$A_{plj}(r,\phi) = \frac{2}{\sqrt{\pi}}\left(\frac{2r^2}{w_0^2}\right)^{l/2}\left[\frac{p!}{(p+l)!}\right]^{1/2} L_p^l\left(\frac{2r^2}{w_0^2}\right)\exp\left(\frac{-r^2}{w_0^2}\right)\times\begin{cases}\exp(+il\phi), j=1\\ \exp(-il\phi), j=2\end{cases} \tag{6}$$

where $p = 0, 1, \ldots$ is the radial index and $l = 0, 1, \ldots$ is the angular index, r is the radial coordinate, ϕ is the angular coordinate, w_0 is the beam waist of the TEM_{00} mode, and $L_p^l(x)$ is the Laguerre polynomials function. There are two forms for the electrical field of LG modes with $l \neq 0$. For simplicity, we use $E_{p,l}$ and $E_{p,-l}$ to express A_{pl1} and A_{pl2}. The electrical field of the vortex array is expressed as a linear combination of $LG_{p,l}$ modes in the form

$$E(r,\phi) = g_1 E_{p1,0}(r,\phi) + g_2 E_{p2,l2}(r,\phi)\, e^{i\theta_2} + g_3 E_{p2,-l2}(r,\phi)\, e^{i\theta_3} + g_4 E_{p3,l3}(r,\phi)\, e^{i\theta_4} + g_5 E_{p3,-l3}(r,\phi)\, e^{i\theta_5} \tag{7}$$

where θ_2, θ_3, θ_4 and θ_5 are the rotation angles of the possible transverse modes $E_{p2,l2}$, $E_{p2,-l2}$, $E_{p3,l3}$, and $E_{p3,-l3}$ participating in formation of stationary patterns, and $\theta_2 + \theta_3 + \theta_4 + \theta_5 = \pi$. g_1, g_2, g_3, g_4 and g_5 are the weights of the transverse modes participating in formation of stationary transverse patterns. Therefore, stationary transverse patterns with different vortex distributions depend on the weights of participating modes, g_1, g_2, g_3, g_4, g_5. The orientation of the transverse patterns of vortex arrays is determined by the particular values of θ_2, θ_3, θ_4, and θ_5.

Although the Yb:YAG microchip laser oscillates in multi-longitudinal modes at different P_{in}s (figure 7), the stationary transverse patterns can be represented as a linear combination of transverse modes belonging to a frequency-degenerated family. Therefore, the stationary transverse patterns formed in the Yb:YAG microchip laser pumped with a tilted annular beam can be obtained theoretically with a set of rate equations with different modal coefficients [19,20]. The theoretically obtained transverse patterns oscillating in TEM_{00} and doughnut modes are shown in figures 2(a2) and (b2), respectively. From figure 2, we can see that the experimentally obtained TEM_{00} mode and doughnut mode are similar to the theoretically obtained patterns. The electrical field of the doughnut-mode beam can be expressed as $E_{0,1}(r,\phi)$ or $E_{0,-1}(r,\phi)$ depending on the helical phases. The transverse patterns of different vortex arrays were theoretically calculated by simultaneously oscillating different transverse modes within the mode-locking regime. The theoretically calculated transverse patterns with different vortex distributions are shown in figure 11. The two-vortex array consisting of two vortices with two opposite helical phases is in simultaneous oscillation of $LG_{1,0}$ mode with two doughnut modes ($LG_{0,1}$ and $LG_{0,-1}$) with different weights and rotation angles. With further increase in the pump power intensity, the $LG_{1,1}$ mode is prior to oscillate other than $LG_{1,0}$ mode. Thus, the three-vortex array is formed with superposition of $LG_{1,1}$ and $LG_{1,-1}$ modes with doughnut modes ($LG_{0,1}$, $LG_{0,-1}$). $LG_{1,0}$ mode and two doughnut modes ($LG_{0,2}$ and $LG_{0,-2}$) belonging to the $2p + l = 2$ frequency-degenerated family are superposed to form four-vortex array [19]. The five-vortex, seven-vortex and nine-vortex arrays are formed with doughnut modes ($LG_{0,3}$, $LG_{0,-3}$), $LG_{1,1}$ and $LG_{1,-1}$ modes belonging to the $2p + l = 3$ frequency-degenerated family. The weights for the four modes depend on the gain profile provided with applied pump power from the tilted annular pump beam. The six-vortex array is a superposition of $LG_{0,2}$, $LG_{0,-2}$, $LG_{1,2}$ and $LG_{1,-2}$ modes. The eight-vortex array is a superposition of $LG_{2,0}$,

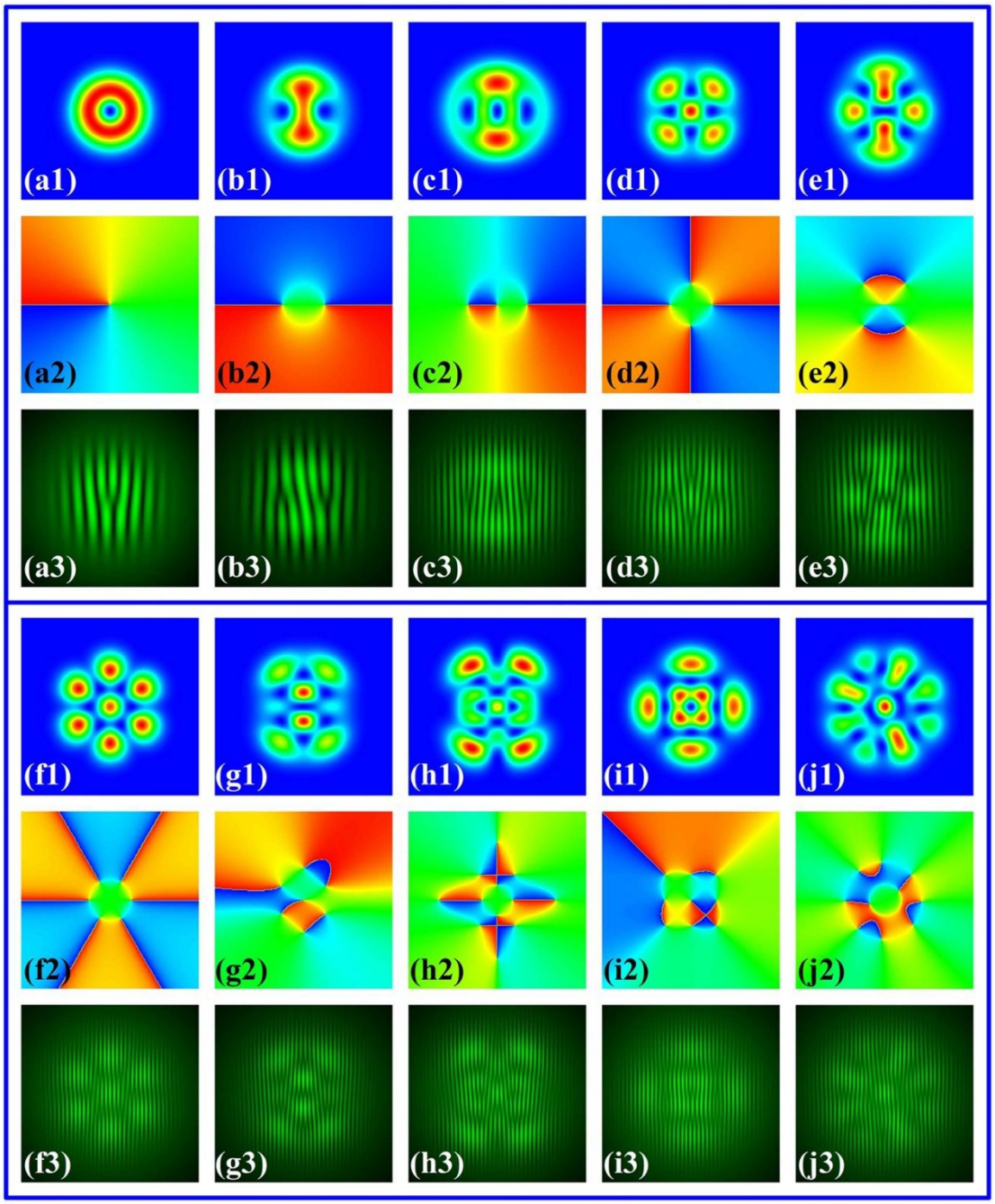

Figure 11. Theoretically calculated transverse patterns (a1)–(j1), phase (a2)–(j2) and interference patterns (a3)–(j3) of vortex arrays with tunable singularities.

$LG_{0,4}$, $LG_{0,-4}$, $LG_{1,2}$ and $LG_{1,-2}$ modes. The ten-vortex array is a superposition of $LG_{2,0}$, $LG_{0,1}$, $LG_{0,-1}$, $LG_{0,4}$ and $LG_{0,-4}$ modes. The transverse modes participating in forming various vortex arrays with tunable phase singularities from 1 to 10 are listed in table 1.

Figures 11(a2)–(j2) show the phase variation of the theoretically calculated vortex arrays. As shown in figure 11(a2), the phase variation of 2π counterclockwise around the vortex clearly confirms that the doughnut vortex has a phase singularity with unitary topological charge. For the two-vortex array, the phase variation of the two vortices is 2π; however, the left one is clockwise varied while the right one is counterclockwise varied, as shown in figure 11(b2). For the three-vortex array, the phase variation of 2π is obtained for three vortices; however, phase varies clockwise for the center vortex, while the other two vary counterclockwise, as shown in figure 11(c2). Similar phase variation of 2π is obtained for the vortices distributed in the vortex arrays with singularities larger than 3, as shown in figures 11(d2)–(j2). The calculated phases provide strong evidence for the vortices distributed in the vortex arrays being phase singularities with unitary topological charge. The theoretically calculated transverse patterns of vortex arrays

with different vortex distributions are in good agreement with the experimental results. The theoretically simulated results strongly support the mechanism of forming vortex arrays with multiple transverse modes oscillating simultaneously by fully using asymmetrical gain distribution in an Yb:YAG crystal pumped with a tilted annular beam.

The theoretically obtained transverse patterns of vortex arrays were used to interfere with a plane-wave reference beam. The calculated interference patterns for various vortex arrays are shown in figures 11(a3)–(j3). A bifurcated forklike interference pattern is obtained for each vortex distributed in the vortex arrays. The directions are opposite for the bifurcated forklike interference patterns of two vortices in the two-vortex array, as shown in figure 11(b3). The direction of one bifurcated forklike interference pattern is opposite to those of the other two for the three-vortex array, as shown in figure 11(c3). Thus, the total charge of the vortices is 0 for the vortex arrays with even vortices. The total charge is ± 1 depending on the phase helicity for the vortex arrays with odd vortices. Good agreement is achieved between experimentally and theoretically calculated interference patterns for some vortex arrays (figure 5). Therefore, the theoretically calculated interference patterns for the vortex arrays further confirm that formation of vortex arrays in an Yb:YAG microchip laser pumped with a tilted annular beam is attributed to the simultaneous oscillation of transverse modes in transverse-mode locking.

5. Conclusions

In summary, direct generation of regular vortex arrays has been demonstrated in an Yb:YAG microchip laser pumped with a tilted annular beam. The number of vortices with unitary topological charge increases linearly with pump power. An increase of pump power leads to the shift of oscillation spectra to lower frequencies. Efficient performance with output power of 2.01 W and optical efficiency of 24.5% has been achieved for a 10-singularity vortex-array laser. Formation of vortex arrays is attributed to multiple transverse-mode oscillation simultaneously supported with asymmetrical gain distribution provided by a tilted annular beam. The theoretically calculated transverse patterns, phases and interference patterns of the vortex arrays formed with linear combination of LG modes are in good agreement with experimentally obtained results. This work provides a flexible and robust method for developing singularity-tunable vortex arrays and structured light control [44] in microchip lasers. The vortex-array lasers with distinct singularity distribution are potential sources for effective trapping microparticles, high-capacity optics communication, and optical modulation.

Acknowledgments

This work was supported by the National Natural Science Foundation of China (61275143 and 61475130) and the Fundamental Research Funds for the Central Universities (20720192020).

ORCID iD

Jun Dong https://orcid.org/0000-0001-7072-5435

References

[1] Allen L, Beijersbergen M W, Spreeuw R J C and Woerdman J P 1992 Orbital angular momentum of light and the transformation of Laguerre–Gaussian laser modes *Phys. Rev.* A **45** 8185–9
[2] Gahagan K T and Swartzlander G A 1996 Optical vortex trapping of particles *Opt. Lett.* **21** 827–9
[3] Grier D G 2003 A revolution in optical manipulation *Nature* **424** 810–6
[4] Zhan Q W 2009 Cylindrical vector beams: from mathematical concepts to applications *Adv. Opt. Photonics* **1** 1–57
[5] Wang J *et al* 2012 Terabit free-space data transmission employing orbital angular momentum multiplexing *Nat. Photon.* **6** 488–96
[6] Gibson G, Courtial J, Padgett M J, Vasnetsov M, Pas'ko V, Barnett S M and Franke-Arnold S 2004 Free-space information transfer using light beams carrying orbital angular momentum *Opt. Express* **12** 5448–56
[7] Fickler R, Lapkiewicz R, Plick W N, Krenn M, Schaeff C, Ramelow S and Zeilinger A 2012 Quantum entanglement of high angular momenta *Science* **338** 640–3
[8] Kozawa Y, Matsunaga D and Sato S 2018 Superresolution imaging via superoscillation focusing of a radially polarized beam *Optica* **5** 86–92
[9] Okulov A Y 2008 3D-vortex labyrinths in the near field of solid-state microchip laser *J. Mod. Opt.* **55** 241–59
[10] Okulov A Y 2019 Configuration of vortex-antivortex lattices at output mirror of wide-area microchip laser *J. Phys.: Conf. Ser.* **1163** 012065
[11] Okulov A Y 2009 Vortex–antivortex wavefunction of a degenerate quantum gas *Laser Phys.* **19** 1796–803
[12] Chen Y F and Lan Y P 2001 Formation of optical vortex lattices in solid-state microchip lasers: spontaneous transverse mode locking *Phys. Rev. A* **64** 063807
[13] Ladavac K and Grier D G 2004 Microoptomechanical pumps assembled and driven by holographic optical vortex arrays *Opt. Express* **12** 1144–9

[14] Woerdemann M, Alpmann C, Esseling M and Denz C 2013 Advanced optical trapping by complex beam shaping *Laser Photonics Rev.* **7** 839–54
[15] Franke-Arnold S, Leach J, Padgett M J, Lembessis V E, Ellinas D, Wright A J, Girkin J M, Ohberg P and Arnold A S 2007 Optical ferris wheel for ultracold atoms *Opt. Express* **15** 8619–25
[16] Li X, Li Y, Zeng X and Han Y 2018 Perfect optical vortex array for optical communication based on orbital angular momentum shift keying *J. Opt.* **20** 125604
[17] Anguita J A, Herreros J and Djordjevic I B 2014 Coherent multimode OAM superpositions for multidimensional modulation *IEEE Photonics J.* **6** 7900811
[18] Forbes A 2019 Structured Light from Lasers *Laser Photonics Rev.* **13** 1900140
[19] Brambilla M, Battipede F, Lugiato L A, Penna V, Prati F, Tamm C and Weiss C O 1991 Transverse laser patterns. I. Phase singularity crystals *Phys. Rev.* A **43** 5090–113
[20] Scheuer J and Orenstein M 1999 Optical vortices crystals: spontaneous generation in nonlinear semiconductor microcavities *Science* **285** 230–3
[21] Barboza R, Bortolozzo U, Assanto G, Vidal-Henriquez E, Clerc M G and Residori S 2013 Harnessing optical vortex lattices in nematic liquid crystals *Phys. Rev. Lett.* **111** 093902
[22] Fuh A Y G, Tsai Y L, Yang C H and Wu S T 2018 Fabrication of optical vortex lattices based on holographic polymer-dispersed liquid crystal films *Opt. Lett.* **43** 154–7
[23] Zhang W H and Chen L X 2018 High-harmonic-generation-inspired preparation of optical vortex arrays with arbitrary-order topological charges *Chin. Opt. Lett.* **16** 030501
[24] Fickler R, Campbell G, Buchler B, Lam P K and Zeilinger A 2016 Quantum entanglement of angular momentum states with quantum numbers up to 10,010 *Proc. Natl Acad. Sci. USA* **113** 13642–7
[25] Ngcobo S, Litvin I, Burger L and Forbes A 2013 A digital laser for on-demand laser modes *Nat. Commun.* **4** 2289
[26] Ricci F, Loffler W and van Exter M P 2012 Instability of higher-order optical vortices analyzed with a multi-pinhole interferometer *Opt. Express* **20** 22961–75
[27] Otsuka K and Chu S C 2009 Generation of vortex array beams from a thin-slice solid-state laser with shaped wide-aperture laser-diode pumping *Opt. Lett.* **34** 10–2
[28] Otsuka K and Chu S C 2017 Spontaneous generation of vortex and coherent vector beams from a thin-slice c-cut Nd: $GdVO_4$ laser with wide-aperture laser-diode end pumping: application to highly sensitive rotational and translational Doppler velocimetry *Laser Phys. Lett.* **14** 075002
[29] Shen Y J, Wan Z S, Fu X, Liu Q and Gong M L 2018 Vortex lattices with transverse-mode-locking states switching in a large-aperture off-axis-pumped solid-state laser *J. Opt. Soc. Am.* B **35** 2940–4
[30] Wan Z S, Shen Y J, Gong M L and Fu X 2018 Quadrant-separable multi-singularity vortices manipulation by coherent superposed mode with spatial-energy mismatch *Opt. Express* **26** 34940–53
[31] Dong J, Wang X L, Zhang M M, Wang X J and He H S 2018 Structured optical vortices with broadband comb-like optical spectra in Yb: $Y_3Al_5O_{12}/YVO_4$ Raman microchip laser *Appl. Phys. Lett.* **112** 161108
[32] Kim J W, Mackenzie J I, Hayes J R and Clarkson W A 2011 High power Er: YAG laser with radially-polarized Laguerre–Gaussian (LG_{01}) mode output *Opt. Express* **19** 14526–31
[33] Fang Z Q, Xia K G, Yao Y and Li J L 2014 Radially polarized LG_{01}-mode Nd: YAG laser with annular pumping *Appl. Phys. B* **117** 219–24
[34] Wei M D, Lai Y S and Chang K C 2013 Generation of a radially polarized laser beam in a single microchip Nd: YVO_4laser *Opt. Lett.* **38** 2443–5
[35] He H S, Chen Z and Dong J 2017 Direct generation of vector vortex beams with switchable radial and azimuthal polarizations in a monolithic Nd: YAG microchip laser *Appl. Phys. Express* **10** 052701
[36] Chen D M, Wang X C, He H S and Dong J 2019 Vector vortices with tunable polarization states directly generated in a microchip laser *Appl. Phys. Express* **12** 052012
[37] Chen D, Miao Y, Fu H, He H, Tong J and Dong J 2019 High-order cylindrical vector beams with tunable topological charge up to 14 directly generated from a microchip laser with high beam quality and high efficiency *APL Photonics* **4** 106106
[38] Pan Y, Zhang M M and Dong J 2019 Orientation and separation controllable dual-vortex passively Q-switched microchip laser *J. Opt.* **21** 085202
[39] Dong J, Bass M, Mao Y L, Deng P Z and Gan F X 2003 Dependence of the Yb^{3+} emission cross section and lifetime on temperature and concentration in yttrium aluminum garnet *J. Opt. Soc. Am.* B **20** 1975–9
[40] Dong J, Shirakawa A, Ueda K, Yagi H, Yanagitani T and Kaminskii A A 2006 Efficient Yb^{3+}: $Y_3Al_5O_{12}$ ceramic microchip lasers *Appl. Phys. Lett.* **89** 091114
[41] Kawase D, Miyamoto Y, Takeda M, Sasaki K and Takeuchi S 2008 Observing quantum correlation of photons in Laguerre–Gauss modes using the Gouy phase *Phys. Rev. Lett.* **101** 050501
[42] Dong J, Shirakawa A and Ueda K-I 2006 Sub-nanosecond passively Q-switched Yb: YAG/Cr^{4+}:YAG sandwiched microchip laser *Appl. Phys.* B **85** 513–8
[43] Kogelnik H and Li T 1966 Laser beams and resonators *Appl. Opt.* **5** 1550–67
[44] Okulov A Y 2020 Structured light entities, chaos and nonlocal maps *Chaos Solitons Fractals* **133** 109638